Effects of Thermal Annealing on the Structural and Electrical Properties of ZnO Thin Films for Boosting their Piezoelectric Response

Quang Chieu Bui, Bassem Salem, Herve Roussel, Xavier Mescot, Youssouf Guerfi, Carmen Jiménez, Vincent Consonni, Gustavo Ardila

Effects of Thermal Annealing on the Structural and Electrical Properties of ZnO Thin Films for Boosting their Piezoelectric Response

Quang Chieu Bui,[1,2,3] Bassem Salem,[2] Hervé Roussel,[3] Xavier Mescot,[1] Youssouf Guerfi,[2] Carmen Jiménez,[3] Vincent Consonni,[3] and Gustavo Ardila.[1]

[1] *Univ. Grenoble Alpes, CNRS, Grenoble INP, IMEP-LAHC, F-38000 Grenoble, France.*

[2] *Univ. Grenoble Alpes, CNRS, LTM, Grenoble INP, F-38054 Grenoble Cedex, France.*

[3] *Univ. Grenoble Alpes, CNRS, Grenoble INP, LMGP, F-38000 Grenoble, France.*

Abstract

The growth process and post-deposition treatment have strong effects on the structure of ZnO thin films, which can also significantly affect their electrical and piezoelectric properties. In this report, the effect of high temperature annealing under oxygen atmosphere on ZnO stacked thin films grown on silicon by pulsed-liquid injection metal-organic chemical vapor deposition is investigated in detail. By varying the annealing temperature from 600 to 1000 °C, the structural analysis reveals the occurrence of *c*-axis oriented grain coarsening and growth processes associated with the improvement of crystallinity and removal of carbon impurities. The electrical resistivity also strongly varies with thermal annealing. Those variations are accompanied by an enhancement of the piezoelectric amplitude measured by piezo-response force microscopy (PFM). Interestingly, the PFM measurements reveal the predominant development of O- and Zn-polar domains at low and high temperature annealing, respectively, originating from the anisotropic grain boundary velocity. The present findings show that the high temperature annealing under oxygen atmosphere in ZnO thin films can enhance not

only its piezo-amplitude but also its Zn-polarity uniformity, which unambiguously leads to the improvement of its piezoelectric performance.

Keywords: Zinc Oxide, Metal-Organic Chemical Vapor Deposition, Annealing, Coalescence, Nanostructures, Piezoelectricity

Introduction

ZnO is not only an abundant, biocompatible material, but also a semiconductor compound possessing many interesting properties that can be used for various applications,[1,2] such as UV light emitting diodes and lasers,[3] UV photodetectors,[4] electron transporting material and transparent conductive oxides in solar cells,[5] or piezoelectric components.[6] The use of ZnO in piezoelectric applications has attracted a lot of attention, in particular because ZnO is an eco-friendly, sustainable material and does not contain lead in contrast to the widely used lead zirconate titanate material.[6,7] The intrinsic piezoelectric property of ZnO results from its non-centrosymmetric wurtzite structure, which is its most stable phase under standard temperature and pressure conditions.[1] ZnO can be integrated in the form of thins films or nanowires into piezoelectric devices, such as surface acoustic wave (SAW) applications,[8] nano-generators and pressure/strain sensors.[9–11] However, the main drawback of ZnO for piezoelectric applications is related to its residual n-type doping.[6,12] The incorporation of many residual impurities (i.e. Al, Ga, In, H…) is typically achieved during the growth of ZnO, regardless of the deposition techniques used.[1,13] These residual impurities can act as shallow donors, generating a large amount of free electrons inside its structure.[1,13] Those free electrons can freely move and screen the piezoelectric potential, in turn reducing drastically its amplitude.[14,15] It is thus essential to reduce the amount of free electrons in order to increase the piezoelectric efficiency. Among the vast number of deposition techniques available to form ZnO thin films and nanowires, metal-organic chemical vapor deposition (MOCVD) offers the great advantages of forming ZnO deposits with a high crystallinity and of monitoring their morphology by simply adjusting the growth temperature,[16–18] the flow rate or the ratio of zinc precursor and oxidizing agent.[19,20] This opens several approaches to tune the properties of ZnO deposits to be suitable for different applications. The morphology transitions from stacked thin films to nanowires through columnar thin films have been revealed in Ref.[18] by increasing growth temperature from 400 to 700 °C. ZnO thin films grown by MOCVD have further been shown to exhibit a high potential for piezoelectric applications.[18,21,22] However, further optimizations of the structural and electrical properties of ZnO thin films to enhance the piezoelectric amplitude are still required.

The effects of thermal annealing on the structural and electrical properties can lead to the performance enhancement of the ferroelectric materials such as PZT,[23] $(Bi_{0.5}Na_{0.5})TiO_3$–$(Bi_{0.5}K_{0.5})TiO_3$–$BaTiO_3$,[24] and $LiNbO_3$,[25] or the piezoelectric materials such as AlN,[26] and ZnO.[27] By using post-deposition thermal annealing under oxygen atmosphere, not only the crystallinity and *c*-axis orientation of ZnO nano-pyramidal structures were improved, but also some defects were removed, resulting in better piezoelectric response as reported in Ref.[27]. Many research groups have studied the effects of thermal annealing on the structural, optical, and electrical properties of ZnO thin films grown by different techniques such as sputtering,[28,29] molecular beam epitaxy,[30] wet chemistry[31] or MOCVD.[32] They have shown that the thermal annealing can improve the crystallinity of ZnO thin films and reduce the density of extended defects in their center. Under oxygen atmosphere, the thermal annealing causes oxygen chemisorption onto grain boundaries, which could lead to the decrease in free charge carrier density and mobility.[32] These consequences would be favorable to improve the piezoelectric performance. However, the effects of thermal annealing on the piezoelectric coefficients, and especially the crystal polarity of ZnO thin films as well as their correlation with the structural and electrical properties have not been investigated yet. The uniformity of the crystal polarity in ZnO thin films is a critical condition for piezoelectric applications as the coexistence of domains with two opposite polarities can neutralize the piezoelectric output of each other. Unlike ferroelectric materials in which the polarity can be reversed and aligned by poling, ZnO is a piezoelectric material and cannot be poled. Therefore, it is crucial to form ZnO thin films not only with a high *c*-axis orientation, but also with a uniform crystal polarity in the final structure to enhance its piezoelectric performance.

In this work, we systematically study the effects of thermal annealing under oxygen atmosphere on the structural, electrical, and piezoelectric properties of ZnO thin films grown by pulsed-liquid injection MOCVD (PLI-MOCVD). By varying the annealing temperature from 600 to 1000 °C, the recrystallization and grain coarsening processes accompanied by the change of electrical resistivity, piezoelectric amplitude, and polarity distribution are described in detail. The structural properties of ZnO thin films are thoroughly investigated by using field-emission scanning electron microscopy (FESEM), X-ray diffraction (XRD), and Raman spectroscopy. Their electrical resistivity and

piezoelectric properties are measured by transmission line measurement (TLM) and piezo-response force microscopy (PFM), respectively.

Experiment

ZnO thin film growth and thermal annealing

ZnO thin films were grown by PLI-MOCVD in an Annealsys MC-200 MOCVD system. Heavily doped p-type Si (100) wafer were used as substrates and as bottom electrode during PFM measurements. The zinc chemical precursor solution used was composed of diethylzinc ($Zn(C_2H_5)_2$, DEZn, Sigma-Aldrich) diluted in cyclohexane at 0.4 mol/l. It was injected to the reactor chamber at a flow rate of 0.5 g/min with 500 sccm Ar as gas carrier. The injection rate for zinc precursor was set at 3 Hz. The O_2 flow rate was set to 500 sccm, corresponding to an O/Zn ratio of about 100. The temperature of the Si substrate and the chamber pressure were maintained at 500 °C and 3 mbar during the growth, respectively. The ZnO thin film grown in 10 minutes has its thickness at of 1100 nm.

The as-grown ZnO thin films were then annealed under oxygen atmosphere at a temperature ranging from 600 to 1000 °C. The thermal annealing was carried out in a horizontal quartz tubular furnace under pure oxygen atmosphere. The pressure in furnace was close to 1 atm. The temperature was ramped up from room temperature to the annealing temperature with a rate of 25 °C/min. Then, the temperature was maintained for 1 hour. Finally, the temperature was cooled down to room temperature naturally.

Structural property measurements

The morphology of ZnO thin films before and after being annealed was investigated by Quanta 250 FEI FEG-SEM. The XRD patterns were recorded by Bruker D8 Advance diffractometer using CuKα1 radiation according to the Bragg-Brentano configuration. Their structural properties were also examined by Raman scattering measurements at room temperature using a Jobin Yvon/Horiba Labram spectrometer with an excitation Ar^+ laser at 488 nm. The cross-polarization (VH) configuration was used in order to reduce the signals from Si substrate.

Electrical property measurements

The resistivity of ZnO thin films was analyzed by using TLM. The metal electrodes, made by 50 nm-thick nickel (Ni) and 120 nm-thick gold (Au) layers, were prepared on the ZnO thin film surface using photolithography, e-beam evaporator and lift-off processes (**Figure S1**). The I-V curves between adjacent electrodes were measured using Karl Suss PM8 system. The total resistance (R_{Total}) obtained from the slope of I-V curves can be expressed as follows:

$$R_{Total} = 2.R_m + 2.R_c + \frac{R_s}{W}.d \quad (1)$$

where R_m is the metallic electrode resistance, R_c is the contact resistance at the electrode/thin film interface, and R_s is the sheet resistance of the thin film; W is the width of the electrode, and d is the distance between electrodes (**Figure S1**). By recording the variation of R_{Total} in function of d and fitting a linear curve, the sheet resistance (R_s) as well as the resistivity of the thin film can be deduced.

Piezoelectric and crystal polarity measurements

The piezoelectric properties of ZnO thin films were analyzed by PFM measurement using Bruker Dimension Icon atomic force microscope equipped with PtSi-NCH tips from Nanosensors, whose spring constant lies in the range of 43 - 50 N/m. The metallic tip was kept in contact with the surface of the thin film during the scanning. Simultaneously, a 5 V AC was applied on the thin film to induce its deformation owing to its piezoelectric property. The amplitude and phase of the deformation were detected by the AFM tip, corresponding to the piezoelectric coefficient and polarity of the thin film, respectively. The frequency of AC voltage was set to 7 kHz to avoid the contact resonance frequency and high background signal contribution as reported in Ref.[33]

Results and discussion

Structural characterization

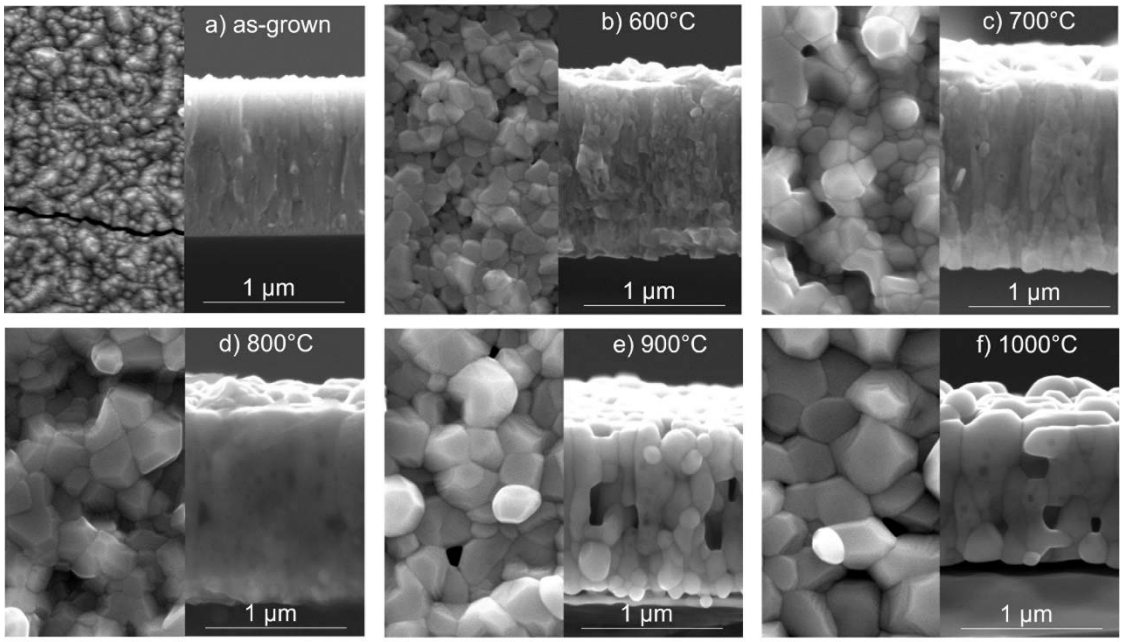

Figure 1. Top- (left) and cross-sectional-view (right) FESEM images of ZnO thin film grown by PLI-MOCVD at 500 °C (a) and ZnO thin films after being annealed at (b) 600, (c) 700, (d) 800, (e) 900, and (f) 1000 °C.

Figure 1 shows the top-view (left) and cross sectional-view (right) FESEM images of ZnO thin films before and after being annealed at different temperatures. From the cross sectional-view image, the as-grown ZnO thin film is found to be composed of stacked grains, as reported in our previous work[18] for that growth temperature of 500 °C. From the top-view images, it can be seen that the grains in all annealed ZnO thin films exhibit a more pronounced hexagonal shape evidencing the wurzite structure, which is the most stable phase of ZnO in these conditions. The average grain size constantly increases from 44 nm in as-grown thin film to 319 nm in 1000 °C-annealed thin film, as presented in **Figure S2**. This shows that grains coalesce and coarsen during an annealing-induced grain growth process to form large-sized grains when the annealing temperature is increased from 600 to 1000 °C. Along with these phenomena, the root mean square roughness measured by AFM also increases from 13 nm in as-grown thin film to 76 nm in 1000 °C-annealed thin film. Grain coarsening and growth

processes are the result of the migration of zinc and oxygen atoms to reduce the density of grain boundary with a higher energy.[34] Simultaneously, the pore coalescence also occurred after thermal annealing, as indicated by the presence of some pores observed in top-view images and some dots with a lower contrast in cross-sectional view images, especially in 900 °C- and 1000 °C-annealed thin films. The similar pore formation in ZnO thin films after thermal annealing has been reported in Refs.[31,35,36]. These pores could affect the electrical properties of ZnO thin films.

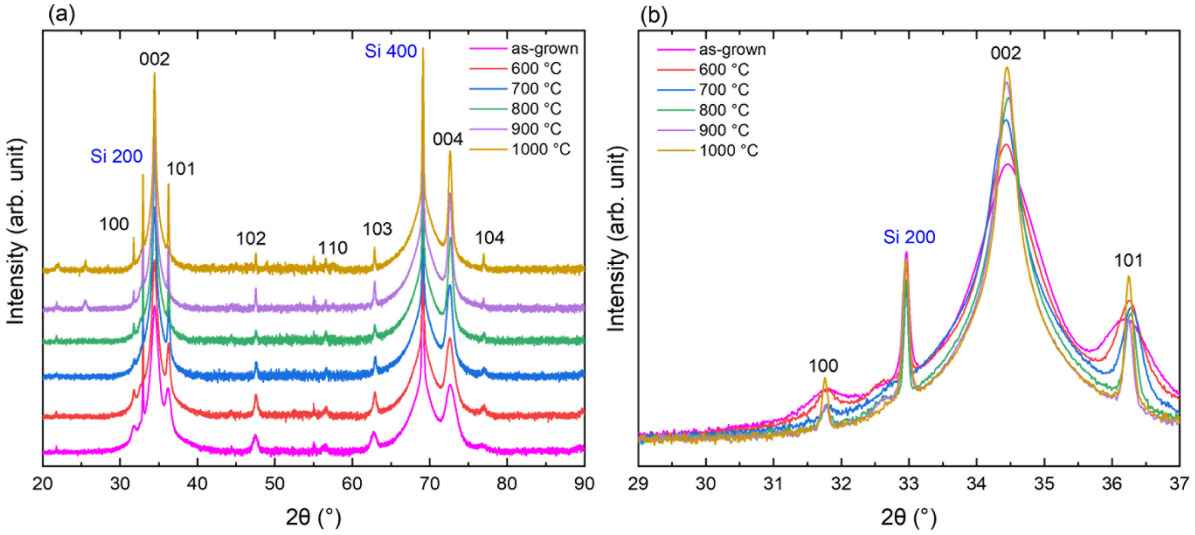

Figure 2. XRD patterns of ZnO thin films plotted in the range of 2θ (a) from 20 to 90° and (b) from 29 to 37° after its intensity normalization using the baseline. The intensity is plotted in logarithm scale.

The ZnO thin films before and after being annealed at various temperatures exhibit similar XRD patterns, as shown in **Figure 2a**, which confirms their wurtzite structure as indicated by the International Center for Diffraction Data (ICDD) file labeled 00-036-1451. Beside the diffraction peaks of Si substrate, the 100, 002, 101, 102, 110, 103, and 104 diffraction peaks of ZnO are located at 31.8, 34.4, 36.3, 47.5, 56.6, 62.9, and 81.4°, respectively. Among them, the intensity of the 002 diffraction peak is much higher than the others, indicating that the ZnO thin films are strongly oriented with the polar *c*-axis normal to the Si substrate surface. As the annealing temperature is raised, the intensity of all ZnO diffraction peaks is significantly increased as revealed in **Figure 2b**, showing the improvement of the crystallinity of the thin films. Concomitantly, the full-width-at-half-maximum

(FWHM) of the diffraction peaks is decreased and its position slightly varies. To get a more reliable and accurate information on the evolution of the grain orientation as a function of the annealing temperature, the texture coefficients C_{hkl} of ZnO thin films for a given (hkl) plane were determined in percent unit by the following equation:[37]

$$C_{hkl}(\%) = \frac{\frac{I_{hkl}}{I_{0,hkl}} \times 100}{\sum_{i=1}^{N} \frac{I_{h_i k_i l_i}}{I_{0,h_i k_i l_i}}} \qquad (2)$$

where I_{hkl} is the hkl peak intensity, $I_{0,hkl}$ is the reference hkl peak intensity from the 00-036-1451 file of the ICDD, and N is the number of peaks considered (N = 6 here).

The FWHM and position of diffraction peaks are also further exploited to assess the homogeneous and inhomogeneous strains, as well as the crystallite size of ZnO thin films and their dependence on the annealing temperature. The homogeneous strain represents the mean residual strain in ZnO thin films at the end of the growth and annealing processes, which lead to the shift of the diffraction peak from its theoretical value in the XRD pattern. The homogeneous strain ε_{hs} in ZnO thin film was calculated as follows:

$$\varepsilon_{hs} = \frac{c - c_o}{c_o} \qquad (3)$$

where c_o is the theoretical *c*-lattice parameter of wurtzite ZnO taken from the 00-036-1451 ICDD file and equal to 5.2066 Å, whereas *c* is the value deduced from the 002 diffraction peak position by using Bragg's law equation:

$$\lambda = 2d \sin\theta \qquad (4)$$

where λ is the wavelength of the Kα1(Cu) source equal to 0.15406 nm, θ is the Bragg angle of the 002 diffraction peak, d is the spacing between (002) planes and equal to half the *c*-lattice parameter in the wurtzite structure.

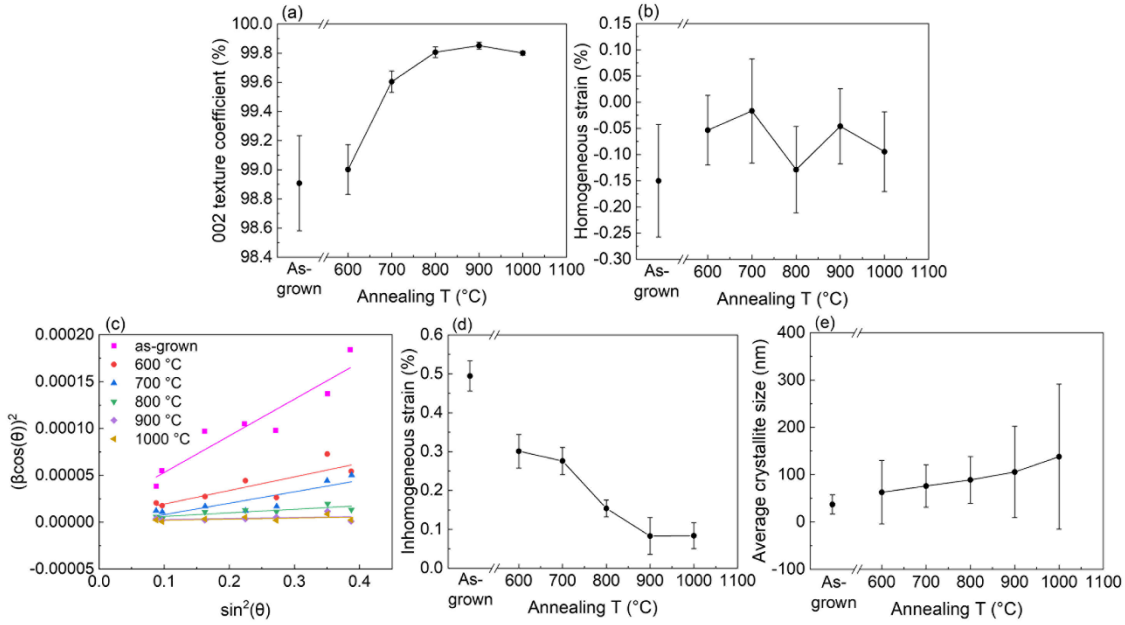

Figure 3. (a) Texture coefficient of the 002 diffraction peak vs annealing temperature. (b) Homogeneous strain vs annealing temperature. (c) Williamson-Hall plot of ZnO thin films. (d) Inhomogeneous strain vs annealing temperature deduced from the Williamson-Hall plot. (e) Average crystallite size vs annealing temperature inferred from the Williamson-Hall plot.

The texture coefficient of the 002 diffraction peak is around 98.9 % in as-grown thin film and increases up to 99.9 % in 900 °C-annealed thin film, as shown in **Figure 3a**. Upon thermal annealing, grains coarsen and the ones with the polar *c*-axis normal to the Si substrate preferentially grow to form large-sized grains at the expense of the grains with other orientations that are progressively consumed. This phenomenon is called abnormal grain growth in polycrystalline thin films[34] and strongly depends on the processing parameters.[38,39] The grain boundary velocity is dependent upon the grain boundary mobility and the difference in the total free energy per unit volume representing the driving force for grain growth, both of them being strongly affected by the grain orientation. As the development of *c*-axis oriented grains exhibiting the highest surface energy is promoted,[40] an anisotropy in the grain boundary mobility is expected here as the dominant mechanism. A slight decrease in the 002 texture coefficient to 99.8% in the 1000 °C-annealed thin film could be due to the deterioration of the structural quality through the formation of large pores, as reported in Ref.[28]. In **Figure 3b**, the

compressive homogeneous strain of -0.15 % in as-grown thin film is measured. For that growth temperature of 500 °C, the homogeneous strain originates from intrinsic stress that is generated during the Volmer-Weber growth mode:[41,42] island nucleation and coalescence at the onset of growth generates high biaxial tensile stress that is relieved and switched to biaxial compressive stress by interface and inclined shears or impurity segregation at grain boundaries. The compressive homogeneous strain decreases down to -0.02 % in 700 °C-annealed thin film owing to grain coarsening and growth. The homogeneous strain, however, suddenly increases to -0.13% in 800 °C-annealed thin films. In that annealing temperature range, the homogeneous strain comes from extrinsic stress, basically thermal stress induced by the thermal expansion coefficient mismatch between ZnO thin film and Si substrate. This can cause a strong residual homogeneous strain after the sample was cooled down from high annealing temperature to room temperature.[28,29] Indeed, the thermal expansion coefficient of hexagonal ZnO in *a*-axis is around 3.2 - 6.05 x 10^{-6} $°C^{-1}$, while the thermal expansion coefficient of Si is 2.5 x 10^{-6} $°C^{-1}$ at room temperature.[43] As the thermal expansion coefficient of ZnO is higher as compared to the Si substrate, ZnO shrinks faster than Si during the cooling down process, resulting in a residual tensile strain in the *a*-axis of ZnO (ε_{xx}) at the interface with the Si substrate, which can be expressed as follows:

$$\varepsilon_{xx} = (\alpha_{ZnO} - \alpha_{Si})\Delta T \quad (5)$$

where α_{ZnO} and α_{Si} are the thermal expansion coefficients of ZnO and Si, respectively, ΔT is temperature difference. From this expression, the residual tensile strain in the *a*-axis of ZnO (ε_{xx}) is calculated to be in the range of 0.05 – 0.28 % when the temperature is cooled down from 800 to 25 °C (room temperature). The tensile strain in the *a*-axis can be converted into the compressive strain in the *c*-axis (ε_{zz}) as follows:[44,45]

$$\varepsilon_{zz} = -2\frac{C_{13}}{C_{33}}\varepsilon_{xx} \quad (6)$$

where C_{13} and C_{33} are elastic constants of ZnO, which are equal to 104.2 and 213.8 GPa, respectively.[46] Thus, the compressive strain along the *c*-axis (ε_{zz}) is estimated to range from -0.27 to -

0.05 %. This compressive strain value is comparable to the homogenous strain deduced from XRD results, indicating that the thermal expansion coefficient mismatch can cause notable residual strain after cooling down process, especially at higher annealing temperature. However, the residual strain decreases again when annealing temperature increased to 900 and 1000 °C. The appearance of pores in these thin films as seen in FESEM images in **Figure 1** could be responsible for this strain relaxation.

Furthermore, the inhomogeneous strain caused by the microstructural defects in the ZnO structure along with the crystallite size were evaluated by using the Williamson-Hall method. The inhomogeneous strain and crystallite size both contribute to the broadening of the diffraction peaks. By considering that the peaks are mainly described by a Gaussian function, their contribution to the FWHM denoted β of diffraction peaks can be expressed as follows:[47]

$$\beta^2 = \beta_S^2 + \beta_D^2 \quad (7)$$

where β is the FWHM of 100, 002, 101, 102, 110, 103, 004 and 104 diffraction peaks, $\beta_S = C\varepsilon_{IS}\tan\theta$ represents the peak broadening contribution from the inhomogeneous strain and $\beta_D = \frac{K\lambda}{Dcos\,\theta}$ represents the peak broadening contribution from the crystallite size, for which θ is the Bragg angle, C is a constant equal to 4, K is a constant depending on the shape of the particles and typically is equal to 0.9,[47] ε_{IS} is the inhomogeneous strain, and L is the average crystallite size. Equation (7) can be rearranged as follows:

$$(\beta\cos\theta)^2 = (C\varepsilon_{IS}\sin\theta)^2 + \left(\frac{K\lambda}{L}\right)^2 \quad (8)$$

By plotting $(\beta\cos\theta)^2$ vs $(\sin\theta)^2$ and fitting linear curves, we can deduce the inhomogeneous strain (ε_{IS}) from the slope and the crystallite size (L) from the intercept, respectively. Since the Williamson-Hall method includes several simplifying assumptions, it is a reliable method to qualitatively assess the evolution of the inhomogeneous strain and crystallite size with the annealing temperature.

The Williamson-Hall plots of ZnO thin films before and after being annealed are shown in **Figure 3c**. The inhomogeneous strain and average crystallite size are presented in **Figures 3d** and **3e**, respectively. In contrast to the evolution of the homogeneous strain, the inhomogeneous strain constantly decreases from 0.49 to 0.08 % (**Figure 3d**) when the annealing temperature increases to 1000 °C. This suggests that a number of extended defects like dislocations and stacking faults are removed at high annealing temperature. The average crystallite size also increases from 37 nm in as-grown thin film up to 138 nm in 1000 °C-annealed thin film (**Figure 3e**). Grain coarsening and growth processes thus occur both in the plane of the film and all along its thickness, as shown by top-view and cross-sectional view FESEM images in **Figure 1**, progressively replacing the stacked thin films to form an almost columnar thin film.[18]

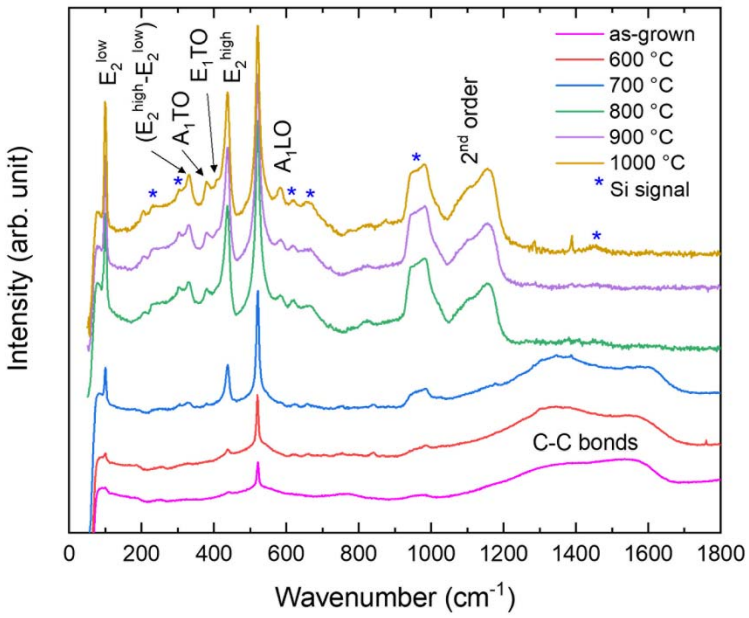

Figure 4. Raman scattering spectra of ZnO thin films. The intensity is plotted in logarithm scale.

Figure 4 shows the Raman scattering spectra of ZnO thin films before and after annealing at different temperatures. The two dominant Raman lines located at 99 and 438 cm^{-1} are assigned to the E_2^{low} and E_2^{high} modes of the ZnO wurtzite structure, respectively.[48] Similarly to the diffraction peaks in the XRD patterns, their intensity significantly increases when the annealing temperature is increased, which again indicates that the crystallinity is largely improved with annealing temperature.

The E_2^{high} line also shifts to the bulk value at 438 cm^{-1} after annealing as shown in **Figure S3**, demonstrating again the strain relaxation. Furthermore, the relative intensity of the E_2^{high} line associated with the oxygen lattice with respect to the E_2^{low} line associated with the zinc lattice continuously increases as the annealing temperature is raised to 1000 °C. This reveals that the oxygen vacancies are progressively filled and vanish as the thermal annealing proceeds. Other Raman lines coming from the ZnO wurtzite structure such as E_2^{high} - E_2^{low}, A_1(TO), E_1(TO) and A_1(LO) located at 333, 378, 410 and 574 cm^{-1}, respectively, are hardly seen in the Raman scattering spectrum of as-grown thin film, but gradually appear when annealing temperature is increased.[48] Notably, two large broad bands centered at around 1360 cm^{-1} and 1580-1600 cm^{-1} are observed in the Raman scattering spectra of the as-grown thin film, which can be assigned to C-C bonds.[49] This indicates that there exist a contamination of carbon in ZnO thin films grown by PLI-MOCVD. The signals from C-C bonds are gradually decreased when annealing temperature is increased and completely vanish at 800 °C, indicating that those carbon contaminations are removed after annealing at sufficient high temperature.

Electrical characterization

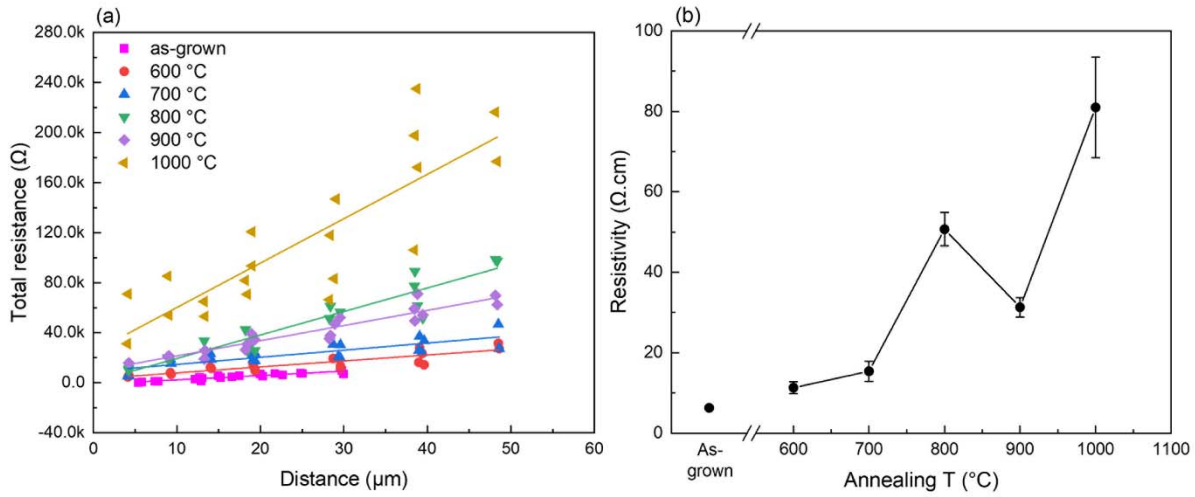

Figure 5. (a) Measured resistance vs distance in transmission line measurement and (b) deduced resistivity of ZnO thin films.

The results of TLM and the deduced electrical resistivity of ZnO thin films as-grown and annealed at different temperatures are presented in **Figure 5**. The electrical resistivity is shown to increase from 6.3 Ω.cm in as-grown thin film to 50.7 Ω.cm in 800 °C-annealed thin film, but then

decreases to 31.3 Ω.cm when annealing temperature was further increased to 900 °C. The electrical resistivity increases again to 81.0 Ω.cm at 1000 °C. The resistivity measurement was repeatedly performed within several months and showed similar results, indicating that the electrical resistivity of ZnO thin films is stable with time.

The variation of the electrical resistivity after annealing can be related to the variation of the charge carrier density and mobility, which are inversely proportional to the electrical resistivity. By increasing annealing temperature, some reports have shown that the resistivity of ZnO increases,[32,50] while other reports have shown that it decreases.[30,35] The increase in the electrical resistivity was explained by i) the atoms relocated during thermal annealing in such a way that a reduced amount of defects that act as shallow donors in ZnO occurs, thus leading to a decrease in the charge carrier density,[50] or by ii) the oxygen adsorbed at the grain boundary after thermal annealing under oxygen atmosphere, creating depletion zones that decrease the charge carrier density and hamper the movement of charge carriers.[32] In other reports, the decrease in the electrical resistivity was explained by the improvement of crystallinity, the decrease of defect density or the decrease of grain boundary density, which helps to reduce the scattering of charge carriers and thus enhance the charge carrier mobility.[30,35] In our case, the electrical resistivity increases when the annealing temperature is increased to 800 °C, which could be due to more oxygen adsorption creating the depletion zone at the grain boundary at higher annealing temperature. Besides, the decrease in the density of defects that can act as shallow donors such as carbon impurities[51] could also be one of the reasons, which is suggested by the decrease of C-C bond signals in Raman spectra (**Figure 4**). These combined effects could cause a large decrease of charge carrier density, leading to an increase in the electrical resistivity when the annealing temperature is increased to 800 °C. Although the charge carrier mobility could also be increased thanks to the grain coarsening and growth processes and to crystallinity improvement with the increase of annealing temperature, it could not overcome the decrease in the charge carrier density. From 800 to 900 °C, the electrical resistivity, however, decreases. Along with this observation, the Raman spectra of 800 °C- and 900 °C-annealed thin films are similar since the C-C bonds signals are completely removed in 800 °C-annealed thin film (**Figure 4**). Because the carbon impurity can act as a

shallow donor,[51] no reduction of C-C bond signals could state that there is no significant decrease of charge carrier density. On the other hand, the charge carrier mobility could continue increasing thanks to the grain coarsening and growth processes along with the crystallinity improvement, as shown in **Figure 3e**. Thus, the electrical resistivity decreases when annealing temperature increased from 800 to 900 °C. At 1000°C, the increase in the electrical resistivity is due to a significant impact of pores that interrupted the charge carrier motion.[35]

Piezoelectric characterization

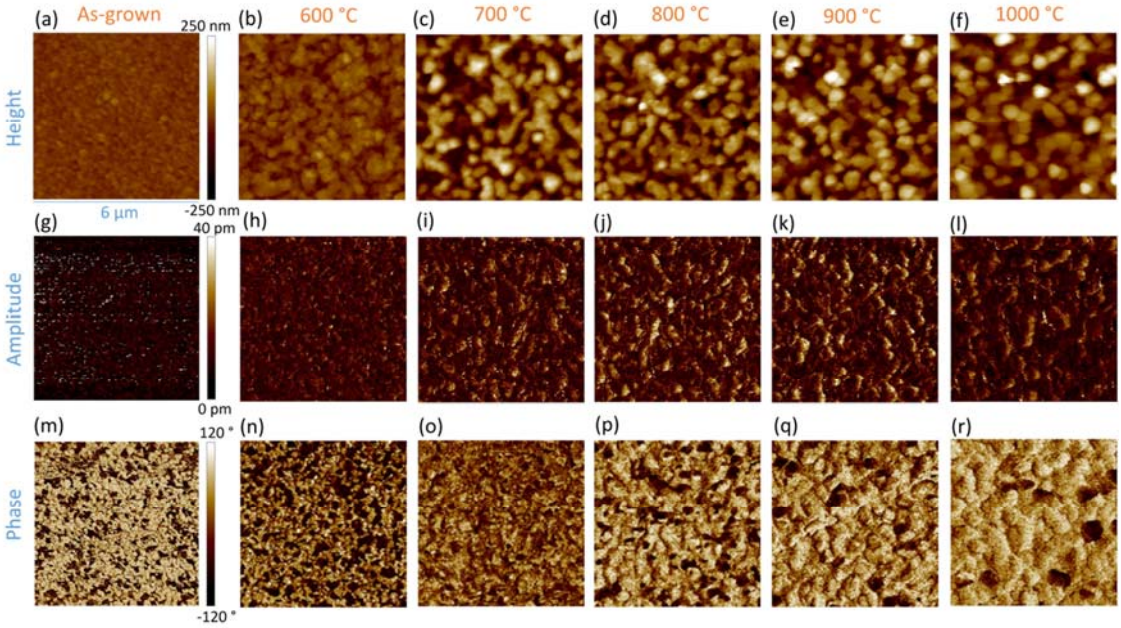

Figure 6. Topography of ZnO thin films (a) before and after being annealed at (b) 600, (c) 700, (d) 800, (e) 900 °C, and (f) 1000 °C. Piezoelectric amplitude of ZnO thin films (g) before and after being annealed at (h) 600, (i) 700, (j) 800, (k) 900 °C, and (l) 1000 °C. Piezoelectric phase of ZnO thin films (m) before and after being annealed at (n) 600, (o) 700, (p) 800, (q) 900 °C, and (r) 1000 °C.

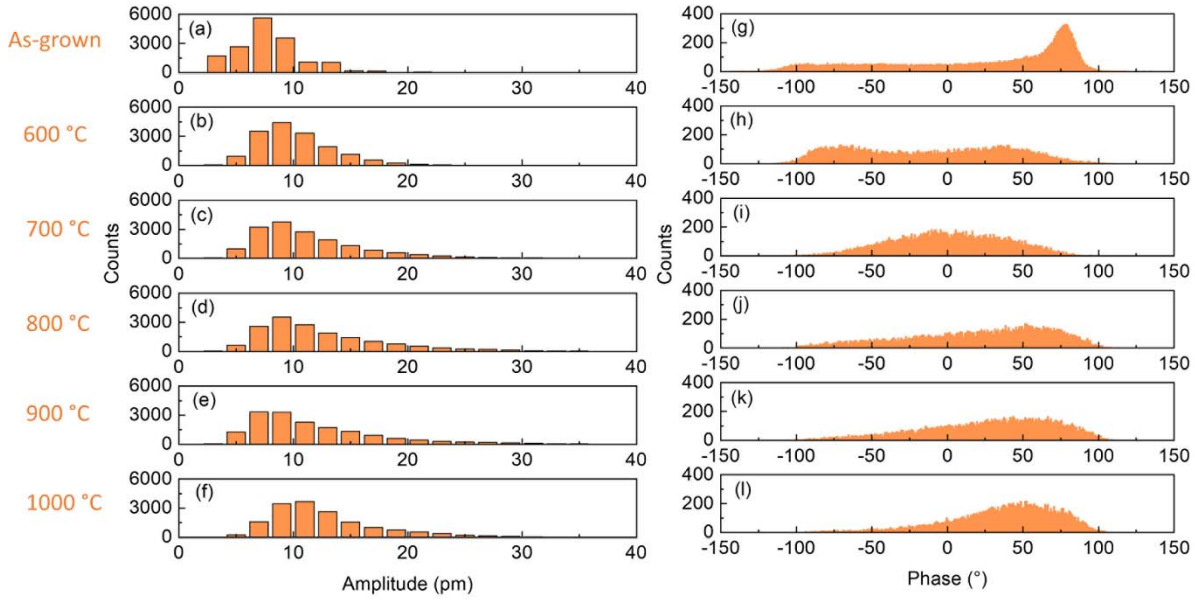

Figure 7. Raw piezoelectric amplitude histograms of ZnO thin films (a) before and after being annealed at (b) 600, (c) 700, (d) 800, (e) 900 and (f) 1000 °C. Raw piezoelectric phase histograms of ZnO thin films (g) before and after being annealed at (h) 600, (i) 700, (j) 800, (k) 900 and (l) 1000 °C.

Figure 6 shows the topography, piezoelectric amplitude and phase images from PFM measurements recorded over a 6 x 6 μm^2 area of the ZnO thin films before and after annealing at different temperatures. The corresponding histograms of piezoelectric amplitude and phase are shown in **Figure 7**. It can be seen that the piezoelectric response in ZnO thin films is inhomogeneous in both amplitude and phase images. The piezoelectric amplitude images as presented in **Figure 6g-l** show that the annealed thin films have a higher piezoelectric amplitude than the as-grown thin film. Also, the thin films annealed at higher temperatures have a larger number of area with higher piezoelectric amplitude than the thin films annealed at lower temperatures. Correlatively, their piezoelectric amplitude histograms shift and stretch to a higher value (**Figure 7a-f**). As the piezoelectric amplitude is proportional to the piezoelectric coefficient, this indicates an increase in the piezoelectric coefficient with the annealing temperature.

In the piezoelectric phase images as presented in **Figure 6m-r**, the area with the phase at around 70 ° (bright area) is attributed to the Zn-polar domains, while the area with the phase at around -90 ° (dark area) is assigned to the O-polar domains.[18] The phases corresponding to the two opposite

piezoelectric polarities of ZnO were confirmed by performing PFM on ZnO monocrystals with an identified polarity.[18] Both dark and bright areas can be seen clearly in the phase response images of the thin films before and after annealing at 600 °C (**Figure 6m-n**). However, it becomes more difficult to distinguish between dark and bright areas in the phase response image of the 700 °C-annealed thin film (**Figure 6o**). At higher annealing temperatures (**Figure 6p-r**), the borders between dark and bright areas can be clearly seen again. Interestingly, the bright area becomes more dominant when the annealing temperature increases. Correspondingly, the negative peak around -90 ° and positive peaks around 70 ° in their phase histograms (**Figure 7g-l**) are assigned to Zn- and O-polar domains, respectively. Both negative and positive peaks can be seen in histograms of as-grown and 600 °C-annealed thin films (**Figure 7g-h**), which relate to Zn- and O-polar domains shown in their phase images (**Figure 6m-n**). Compared to the as-grown thin film, the thin film annealed at 600 °C has its phase histogram distribution reduced on the positive side and increased on the negative side. This reveals that the O-polar domains in the thin film are more developed after being annealed at 600 °C. In 700 °C-annealed thin film, a broad peak centered at nearly 0 ° is shown in its histogram (**Figure 7i**), corresponding to the dark-bright mixed areas that are observed in its phase image (**Figure 6o**). This could be explained by the coarsening process between grains with Zn- and O-polarity upon thermal annealing. As they are of opposite polarities, the coarsening and growth processes result in the formation of domains with compensated polarity, in which there is no piezoelectric signal. The phase response of non-piezoelectric area, which has a large area in 700 °C-annealed thin film, can be randomly distributed from negative to positive values, leading to a broad peak centered at 0 ° in its histogram, as seen in **Figure 7i**. In the thin films annealed at higher temperature, their phase responses are distributed more on the positive side (**Figure 7j-l**), exhibiting that the Zn-polar domains are predominant over the O-polar domains. This indicates that the grains with Zn-polarity prevailed over the grains with O-polarity after the grain coarsening and growth processes at high annealing temperature. Given that the surface energy of Zn-polar *c*-plane is significantly larger than the surface energy of O-polar *c*-plane,[52] this supports again that the grain coarsening and growth processes at high temperatures is driven by an anisotropy in the grain boundary mobility rather than in the minimization of the free energy per unit volume governed by the surface energy contribution.[34]

Furthermore, the PFM data was treated to separate the piezoelectric responses of the Zn- and O-polar domains, and to remove noise from non-polarity areas. The data treatment is described as follows: data points with the phase response higher than 50 ° were assigned to Zn-polar domains and kept without modification; in contrast, data points with the phase response lower than -50 ° were assigned to O-polar domains and had their amplitude value multiplied by -1. Other data points were assigned to non-polarity areas and were removed.

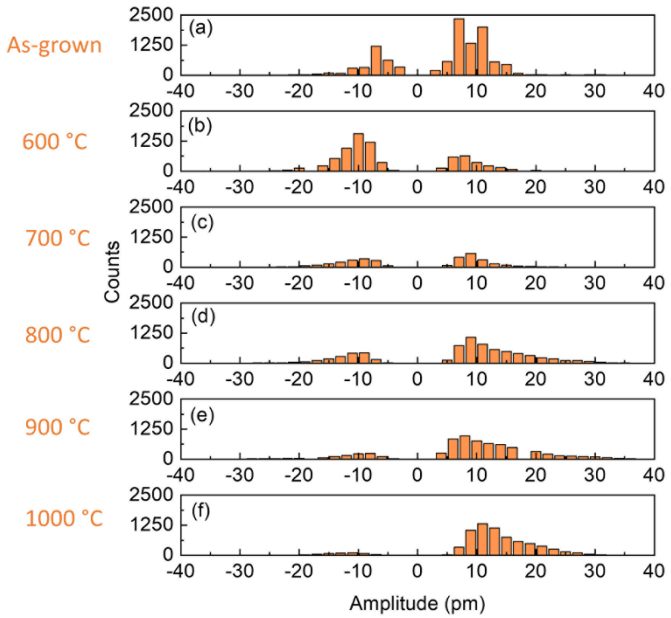

Figure 8. Piezoelectric amplitude histograms of ZnO thin films (a) before and after being annealed at (b) 600, (c) 700, (d) 800, (e) 900 and (f) 1000 °C after the data treatments.

Figure 8 shows piezoelectric amplitude histograms after data treatment of ZnO thin films before and after annealing at different temperatures. These results show that the area of Zn-polar domains decreases in thin films annealed at 600 and 700 °C (**Figure 8a-c**), but increases again in thin films annealed at 800, 900, and 1000 °C (**Figure 8d-f**). The piezoelectric amplitude distribution of the Zn-polar domains also stretches to higher value in those high temperature annealed thin films (**Figure 8d-f**). On the other hand, the O-polar domains have its piezoelectric amplitude and area increased in the 600 °C-annealed thin film, but then its area decreases as being compensated by the Zn-polar

domains in 700 °C-annealed thin film and being consumed at higher annealing temperature (**Figure 8d**).

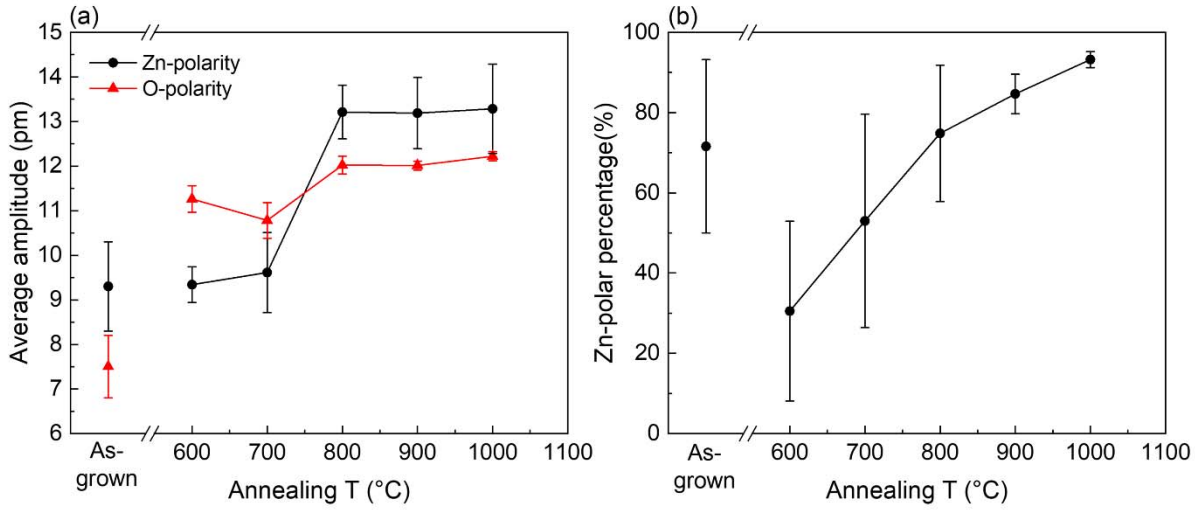

Figure 9. Average piezoelectric amplitude on (a) Zn-polar and O-polar area, and (b) percentage of Zn-polar area of ZnO thin films.

The average piezoelectric amplitude responses of the Zn- and O-polar domains, along with the area percentage of the Zn-polar domains after removing non-polar areas are presented in **Figure 9**. The average piezoelectric amplitude response of the Zn-polar domains retains a value close to 9.5 pm in as-grown and annealed thin films up to 700 °C, and then increases significantly to 13.2 pm at 800 °C (**Figure 9a**). At the same time, the average piezoelectric amplitude response of the O-polar domains increases from a smaller value of 7.5 pm in the as-grown thin film to 11.3 pm in the thin film annealed at 600 °C. It then decreases slightly to 10.8 pm at 700 °C, and eventually increases slightly to 12 pm at 800 °C (**Figure 9a**). The average piezoelectric amplitude of both polar domains does not change at the annealing temperatures above 800 °C. It should be noted that the bottom electrode used in this report is highly doped Si substrate. We suspect that, after annealing at 1000 °C, the substrate was partially oxidized, and ZnO thin films started being peeled off the substrate. This could cause poor electrical contact between the ZnO thin film and bottom electrode, leading to an underestimation of the piezoelectric amplitude of this sample. The area percentage of the Zn-polar domains decreases from 71.7 % in the as-grown thin film to 30.5 % in the thin film annealed at 600 °C, but then increases constantly up to 93.2 % at 1000 °C (**Figure 9b**). These results again indicate that i) the piezoelectric

amplitude in both polar domains increases with annealing temperature, and that ii) the Zn-polar domains becomes dominant after annealing at high temperature. The increase in the piezoelectric amplitude with annealing temperature could be due to the larger vertical alignment of the *c*-axis oriented domains in the ZnO thin films annealed at higher temperature, as suggested in the XRD patterns (**Figure 3a**).[27] Another explanation could be related to the decrease in the charge carrier density after annealing at higher temperature as suggested in the TLM method (**Figure 5**), leading to a reduction of the screening effect.[27] These effects appear to be more pronounced in the case of the Zn-polar domains than in the case of the O-polar domains. The predominance of the O- and Zn-polar domains after annealing at low and high temperatures can be explained as follows. In the low annealing temperature range, a faster coarsening and growth rate of the O-polar grains as compared to the Zn-polar grains occurs, because the development of the O-polar domains with the lower surface energy[52] is favorable for minimizing the free energy of the system and hence boosting the driving force for grain growth. In contrast, in the high annealing temperature range, a faster coarsening and growth rate of the Zn-polar grains as compared to the O-polar grains takes place owing to the predominant anisotropy in the grain boundary mobility. A comparison between the migration rates of grain boundary along Zn- and O-polarity was demonstrated in Ref. [53]. Their results showed that the migration rate is significantly faster in the Zn-polar domains than in the O-polar domains, which validates the present considerations. As a consequence, the development of polar domains upon thermal annealing in the ZnO stacked thin films is governed by the annealing temperature-dependent competitive process between the difference in the free energy per unit volume and the grain boundary mobility, both of them being strongly anisotropic. Overall, the prevalence of Zn-polar domains with a larger piezoelectric amplitude after high temperature annealing can lead to the polarity uniformity in ZnO stacked thin films grown by MOCVD, which significantly enhances its piezoelectric performance.

Conclusion

In summary, we have demonstrated the effect of high temperature annealing under oxygen atmosphere on the structural, electrical, and piezoelectric properties of ZnO stacked thin films grown by PLI-

MOCVD. By varying the annealing temperature from 600 to 1000 °C, the *c*-axis oriented grain coarsening and growth processes along with the highly improvement of crystallinity has been observed. A large amount of remaining carbon impurity from the growth process has also been removed after annealing. At the same time, the electrical resistivity has significantly been affected by the annealing process. Those reasons could explain the increase of piezoelectric amplitude with the annealing temperature. Interestingly, the PFM measurement also revealed that grains with O- and Zn-polarity have become predominant after the coarsening and growth processes at low and high annealing temperature, respectively, which has led to polarity uniformity. An annealing temperature-dependent competitive process between the difference in the anisotropic free energy per unit volume and the anisotropic grain boundary mobility has been discussed to account for the dominant O- and Zn-polarity, respectively. The post-deposition thermal annealing of ZnO thin films not only enhances its *c*-axis orientation, but also its polarity uniformity, which are two critical conditions for enhancing the performances of piezoelectric applications. These results have shown a strong correlation of the structural, electrical and piezoelectric properties of ZnO thin films and point out that high temperature annealing under oxygen atmosphere can significantly improve its piezoelectric performance.

Acknowledgements

This work was supported by the French National Research Agency in the framework of the "Investissements d'avenir" program (ANR-15-IDEX-02) through the project CDP NEED. Q.C.B. held a doctoral fellowship from the project CDP NEED. The authors further acknowledge the support from the CNRS Renatech Network through the "Plateforme Technologique Amont" in a cleanroom environment. This research has also benefited from some of the characterization equipments of the Grenoble INP-CMTC platform. The authors are further grateful to Odette Chaix-Pluchery, LMGP, Grenoble, France, for her assistance in the Raman spectroscopy. This work benefited from the facilities and expertise of the OPE)N(RA characterization platform of FMNT (FR 2542, fmnt.fr) supported by CNRS, Grenoble INP and UGA.

References

(1) Özgür, Ü.; Alivov, Y. I.; Liu, C.; Teke, A.; Reshchikov, M. A.; Doğan, S.; Avrutin, V.; Cho, S. J.; Morkoç, H. A Comprehensive Review of ZnO Materials and Devices. *J. Appl. Phys.* **2005**, *98* (4), 041301. https://doi.org/10.1063/1.1992666.

(2) Kołodziejczak-radzimska, A.; Jesionowski, T. Zinc Oxide—From Synthesis to Application: A Review. *Materials (Basel).* **2014**, *7* (4), 2833–2881. https://doi.org/10.3390/ma7042833.

(3) Willander, M.; Nur, O.; Zhao, Q. X.; Yang, L. L.; Lorenz, M.; Cao, B. Q.; Pérez, J. Z.; Czekalla, C.; Zimmermann, G.; Grundmann, M.; et al. Zinc Oxide Nanorod Based Photonic Devices : Recent Progress in Growth , Light Emitting Diodes and Lasers. *Nanotechnology* **2009**, *20* (33), 332001. https://doi.org/10.1088/0957-4484/20/33/332001.

(4) Tian, W.; Lu, H.; Li, L. Nanoscale Ultraviolet Photodetectors Based on One- Dimensional Metal Oxide Nanostructures. *Nano Res.* **2015**, *8* (2), 382–405. https://doi.org/10.1007/s12274-014-0661-2.

(5) Consonni, V.; Briscoe, J.; Kärber, E.; Li, X.; Cossuet, T. ZnO Nanowires for Solar Cells : A Comprehensive Review. *Nanotechnology* **2019**, *30* (36), 362001.

(6) Wang, Z. L. Towards Self-Powered Nanosystems : From Nanogenerators to Nanopiezotronics **. *Adv. Funct. Mater.* **2008**, *18*, 3553–3567. https://doi.org/10.1002/adfm.200800541.

(7) Wei, H.; Wang, H.; Xia, Y.; Cui, D.; Shi, Y.; Dong, M.; Liu, C.; Ding, T.; Zhang, J.; Ma, Y.; et al. An Overview of Lead-Free Piezoelectric Materials and Devices. *J. Mater. Chem. C* **2018**, *6* (46), 12446. https://doi.org/10.1039/c8tc04515a.

(8) Yildirim, B.; Tigli, O. Comprehensive Characterization of ZnO Thin Films for Surface Acoustic Wave Applications. *J. Mater. Sci. Mater. Electron.* **2019**, *30*, 14621–14630. https://doi.org/10.1007/s10854-019-01834-8.

(9) Briscoe, J.; Dunn, S. Piezoelectric Nanogenerators – a Review of Nanostructured Piezoelectric Energy Harvesters. *Nano Energy* **2015**, *14*, 15–29. https://doi.org/10.1016/j.nanoen.2014.11.059.

(10) Tao, R.; Parmar, M.; Ardila, G.; Oliveira, P.; Marques, D.; Montès, L.; Mouis, M. Performance of ZnO Based Piezo-Generators under Controlled Compression. *Semicond. Sci. Technol.* **2017**, *32* (6), 064003.

(11) Parmar, M.; Leon Perez, E. A. A.; Ardila, G.; Saoutieff, E.; Pauliac-Vaujour, E.; Mouis, M. A Demonstration of the Mechanical Sensing Capability of Individually Contacted Vertical Piezoelectric Nanowires Arranged in Matrices. *Nano Energy* **2019**, *56*, 859–867. https://doi.org/10.1016/j.nanoen.2018.11.088.

(12) Liu, C.; Peng, M.; Yu, A.; Liu, J.; Song, M.; Zhang, Y.; Zhai, J. Interface Engineering on P-CuI/n-ZnO Heterojunction for Enhancing Piezoelectric and Piezo-Phototronic Performance. *Nano Energy* **2016**, *26*, 417–424. https://doi.org/10.1016/j.nanoen.2016.05.041.

(13) Janotti, A.; Van De Walle, C. G. Fundamentals of Zinc Oxide as a Semiconductor. *Reports Prog. Phys.* **2009**, *72* (12), 126501. https://doi.org/10.1088/0034-4885/72/12/126501.

(14) Wang, Z. L.; Song, J. Piezoelectric Nanogenerators Based on Zinc Oxide Nanowire Arrays. *Science (80-.).* **2006**, *312* (5771), 242–246. https://doi.org/10.1126/science.1124005.

(15) Tao, R.; Mouis, M.; Ardila, G. Unveiling the Influence of Surface Fermi Level Pinning on the Piezoelectric Response of Semiconducting Nanowires. *Adv. Electron. Mater.* **2017**, *4* (1), 1700299. https://doi.org/10.1002/aelm.201700299.

(16) Park, J. Y.; Lee, D. J.; Yun, Y. S.; Moon, J. H.; Lee, B.; Kim, S. S. Temperature-Induced Morphological Changes of ZnO Grown by Metalorganic Chemical Vapor Deposition. *J. Cryst. Growth* **2005**, *276* (1), 158–164. https://doi.org/10.1016/j.jcrysgro.2004.11.326.

(17) Malandrino, G.; Blandino, M.; Fragala, M. E.; Losurdo, M.; Bruno, G. Relationship between Nanostructure and Optical Properties of ZnO Thin Films. *J. Phys. Chem. C* **2008**, *112* (26), 9595–9599.

(18) Bui, Q. C.; Ardila, G.; Sarigiannidou, E.; Roussel, H.; Jimenez, C.; Chaix-Pluchery, O.; Guerfi, Y.; Bassani, F.; Donatini, F.; Mescot, X.; et al. Morphology Transition of ZnO from Thin Film to Nanowires on Silicon and Its Correlated Enhanced Zinc Polarity Uniformity and Piezoelectric Responses. *ACS Appl. Mater. Interfaces* **2020**, *12* (26), 29583−29593. https://doi.org/10.1021/acsami.0c04112.

(19) Fanni, L.; Aebersold, A. B.; Morales-masis, M.; Alexander, D. T. L.; Hessler-wyser, A.; Nicolay, S. Increasing Polycrystalline Zinc Oxide Grain Size by Control of Film Preferential Orientation. *Cryst. Growth Des.* **2015**, *15* (12), 5886–5891. https://doi.org/10.1021/acs.cgd.5b01299.

(20) Aebersold, A. B.; Fanni, L.; Hessler-wyser, A.; Nicolay, S.; Alexander, D. T. L.; Ballif, C. Quantifying Competitive Grain Overgrowth in Polycrystalline ZnO Thin Fi Lms. *Acta Mater.* **2019**, *173*, 74–86.

(21) Emanetoglu, N. W.; Gorla, C.; Liu, Y.; Liang, S.; Y.Lu. Epitaxial ZnO Piezoelectric Thin Films for Saw Filters. *Mater. Sci. Semicond. Process.* **1999**, *2* (3), 247–252. https://doi.org/10.1111/j.1467-9655.2007.00439_8.x.

(22) Khomchenko, V. S.; Roshchina, N. N.; Zavyalova, L. V; Strelchuk, V. V; Svechnikov, G. S.; Tatyanenko, N. P.; Gromashevskii, V. L.; Litvin, O. S.; Avramenko, E. A.; Snopok, B. A. Structure and the Emission and Piezoelectric Properties of MOCVD Grown ZnS , ZnS – ZnO , and ZnO Films. *Tech. Phys.* **2014**, *59* (1), 93–101. https://doi.org/10.1134/S1063784214010071.

(23) Smith, G. L.; Pulskamp, J. S.; Sanchez, L. M.; Potrepka, D. M.; Proie, R. M.; Ivanov, T. G.;

Rudy, R. Q.; Nothwang, W. D.; Bedair, S. S.; Meyer, C. D.; et al. PZT-Based Piezoelectric MEMS Technology. *J. Am. Ceram. Soc.* **2012**, *95* (6), 1777–1792. https://doi.org/10.1111/j.1551-2916.2012.05155.x.

(24) Zhan, K.; Su, M.; Han, H.; Xie, S. F.; Zhu, Y. K.; Wang, D.; Cheng, H. B.; Wang, X. Y. Effect of Annealing Temperature on Piezoelectric and Mechanical Properties of (Bi0.5Na0.5)TiO3–(Bi0.5K0.5)TiO3–BaTiO3 Thin Film. *Ceram. Int.* **2016**, *42* (1), 1627–1632. https://doi.org/10.1016/j.ceramint.2015.09.114.

(25) Bhagavannarayana, G.; Budakoti, G. C.; Maurya, K. K.; Kumar, B. Enhancement of Crystalline , Piezoelectric and Optical Quality of LiNbO3 Single Crystals by Post-Growth Annealing and Poling. *J. Chem. Phys.* **2005**, *282* (3–4), 394–401. https://doi.org/10.1016/j.jcrysgro.2005.05.025.

(26) Vergara, L.; Olivares, J.; Iborra, E.; Clement, M.; Sanz-Hervás, A.; Sangrador, J. Effect of Rapid Thermal Annealing on the Crystal Quality and the Piezoelectric Response of Polycrystalline AlN Films. *Thin Solid Films* **2006**, *515* (4), 1814–1818. https://doi.org/10.1016/j.tsf.2006.07.002.

(27) Lim, T.; Ico, G.; Jung, K.; Bozhilov, K. N.; Nam, J.; Martinez-Morales, A. A. Crystal Growth and Piezoelectric Characterization of Mechanically Stable ZnO Nanostructure Arrays. *CrystEngComm* **2018**, *20* (38), 5688. https://doi.org/10.1039/c8ce00799c.

(28) Fang, Z. B.; Yan, Z. J.; Tan, Y. S.; Liu, X. Q.; Wang, Y. Y. Influence of Post-Annealing Treatment on the Structure Properties of ZnO Films. *Appl. Surf. Sci.* **2005**, *241* (3–4), 303–308. https://doi.org/10.1016/j.apsusc.2004.07.056.

(29) Daniel, G. P.; Justinvictor, V. B.; Nair, P. B.; Joy, K.; Koshy, P.; Thomas, P. V. Effect of Annealing Temperature on the Structural and Optical Properties of ZnO Thin Films Prepared by RF Magnetron Sputtering. *Phys. B Condens. Matter* **2010**, *405* (7), 1782–1786.

https://doi.org/10.1016/j.physb.2010.01.039.

(30) Ogata, K.; Sakurai, K.; Fujita, S.; Fujita, S.; Matsushige, K. Effects of Thermal Annealing of ZnO Layers Grown by MBE. *J. Cryst. Growth* **2000**, *214–215*, 312–315.

(31) Richardson, J. J.; Goh, G. K. L.; Le, H. Q.; Liew, L.; Lange, F. F.; Denbaars, S. P. Thermally Induced Pore Formation in Epitaxial ZnO Films Grown from Low Temperature Aqueous Solution. *Cryst. Growth Des.* **2011**, *11* (8), 3558–3563. https://doi.org/10.1021/cg200528e.

(32) Gritsenko, L. V; Abdullin, K. A.; Gabdullin, M. T.; Kalkozova, Z. K.; Kumekov, S. E.; Mukash, Z. O.; Sazonov, A. Y.; Terukov, E. I. Effect of Thermal Annealing on Properties of Polycrystalline ZnO Thin Films. *J. Cryst. Growth* **2017**, *457*, 164–170. https://doi.org/10.1016/j.jcrysgro.2016.07.026.

(33) Jungk, T.; Hoffmann, Á.; Soergel, E. Quantitative Analysis of Ferroelectric Domain Imaging with Piezoresponse Force Microscopy. *Appl. Phys. Lett.* **2006**, *89* (16), 163507. https://doi.org/10.1063/1.2362984.

(34) Thompson, C. V. Structure Evolution during Processing of Polycrystalline Films. *Annu. Rev. Mater. Sci.* **2000**, *30*, 159–190.

(35) Yi, G. R.; Kim, H. S.; Lee, D. H.; Kim, B.; Kim, C. K. Effect of Annealing on Performance of ZnO Thin Film Transistors. *Mol. Cryst. Liq. Cryst.* **2019**, *678* (1), 43–52. https://doi.org/10.1080/15421406.2019.1597527.

(36) Nijikovsky, B.; Richardson, J. J.; Garbrecht, M.; DenBaars, S. P.; Kaplan, W. D. Microstructure of ZnO Films Synthesized on MgAl2O4 from Low-Temperature Aqueous Solution : Growth and Post-Annealing. *J. Mater. Sci.* **2013**, *48*, 1614–1622. https://doi.org/10.1007/s10853-012-6918-9.

(37) Consonni, V.; Feuillet, G.; Gergaud, P. Plasticity Induced Texture Development in Thick

Polycrystalline CdTe : Experiments and Modeling. *J. Appl. Phys.* **2008**, *103* (6), 063529. https://doi.org/10.1063/1.2895382.

(38) Consonni, V.; Rey, G.; Roussel, H.; Bellet, D. Thickness Effects on the Texture Development of Fluorine-Doped SnO2 Thin Films : The Role of Surface and Strain Energy. *J. Appl. Phys.* **2012**, *111* (3), 033523. https://doi.org/10.1063/1.3684543.

(39) Consonni, V.; Rey, G.; Roussel, H.; Doisneau, B.; Blanquet, E.; Bellet, D. Preferential Orientation of Fluorine-Doped SnO2 Thin Films : The Effects of Growth Temperature. *Acta Mater.* **2013**, *61* (1), 22–31. https://doi.org/10.1016/j.actamat.2012.09.006.

(40) Wander, A.; Schedin, F.; Steadman, P.; Norris, A.; Mcgrath, R.; Turner, T. S.; Thornton, G.; Harrison, N. M. Stability of Polar Oxide Surfaces. *Phys. Rev. Lett.* **2001**, *86* (17), 3811. https://doi.org/10.1103/PhysRevLett.86.3811.

(41) Nix, W. D.; Clemens, B. M. Crystallite Coalescence: A Mechanism for Intrinsic Tensile Stresses in Thin Films. *J. Mater. Res.* **1999**, *14* (8), 3467–3473.

(42) Floro, J. A.; Hearne, S. J.; Hunter, J. A.; Kotula, P.; Chason, E.; Seel, S. C.; Thompson, C. V. The Dynamic Competition between Stress Generation and Relaxation Mechanisms during Coalescence of Volmer – Weber Thin Films. *J. Appl. Phys.* **2001**, *89* (9), 4886. https://doi.org/10.1063/1.1352563.

(43) Jou, J.-H.; Han, M.-Y.; Cheng, D.-J. Substrate Dependent Internal Stress in Sputtered Zinc Oxide Thin Films. *J. Appl. Phys.* **1992**, *71* (9), 4333.

(44) Wright, A. F. Elastic Properties of Zinc-Blende and Wurtzite AlN, GaN, and InN. *J. Appl. Phys.* **1997**, *82* (6), 2833.

(45) Wagner, J.; Bechstedt, F. Properties of Strained Wurtzite GaN and AlN : Ab Initio Studies. *Phys. Rev. B* **2002**, *66* (11), 115202. https://doi.org/10.1103/PhysRevB.66.115202.

(46) Hong, R.; Shao, J.; He, H.; Fan, Z. Influence of Buffer Layer Thickness on the Structure and Optical Properties of ZnO Thin Films. *Appl. Surf. Sci.* **2006**, *252* (8), 2888–2893. https://doi.org/10.1016/j.apsusc.2005.04.041.

(47) Mote, V. D.; Purushotham, Y.; Dole, B. N. Influence of Post-Annealing Treatment on the Structure. *J. Theor. Appl. Phys.* **2012**, *6* (6).

(48) Cuscó, R.; Alarcón-lladó, E.; Ibáñez, J.; Artús, L.; Jiménez, J.; Wang, B.; Callahan, M. J. Temperature Dependence of Raman Scattering in ZnO. *Phys. Rev. B* **2007**, *75* (16), 165202. https://doi.org/10.1103/PhysRevB.75.165202.

(49) Ferrari, A. C.; Robertson, J. Interpretation of Raman Spectra of Disordered and Amorphous Carbon. *Phys. Rev. B* **2000**, *61* (20), 14095.

(50) Asghar, M.; Noor, H.; Awan, M. S.; Naseem, S.; Hasan, M.-A. Post-Annealing Modification in Structural Properties of ZnO Thin Films on p-Type Si Substrate Deposited by Evaporation. *Mater. Sci. Semicond. Process.* **2008**, *11* (1), 30–35. https://doi.org/10.1016/j.mssp.2008.07.008.

(51) Mohammadbeigi, F.; Senthil Kumar, E.; Alagha, S.; Anderson, I.; Watkins, S. P. Carbon Related Donor Bound Exciton Transitions in ZnO Nanowires. *J. Appl. Phys.* **2014**, *116* (5), 053516. https://doi.org/10.1063/1.4892090.

(52) Tang, C.; Spencer, M. J. S.; Barnard, A. S. Activity of ZnO Polar Surfaces: An Insight from Surface Energies. *Phys. Chem. Chem. Phys.* **2014**, *16* (40), 22139–22144. https://doi.org/10.1039/c4cp03221g.

(53) Lee, J.; Wiederhorn, S. M. Effects of Polarity on Grain-Boundary Migration in ZnO. *J. Am. Ceram. Soc.* **2004**, *87* (7), 1319–1323.

Figure Legends

Figure 1. Top- (left) and cross-sectional-view (right) FESEM images of ZnO thin film grown by PLI-MOCVD at 500 °C (a) and ZnO thin films after being annealed at (b) 600, (c) 700, (d) 800, (e) 900, and (f) 1000 °C.

Figure 2. XRD patterns of ZnO thin films plotted in the range of 2θ (a) from 20 to 90° and (b) from 29 to 37° after its intensity normalization using the baseline. The intensity is plotted in logarithm scale.

Figure 3. (a) Texture coefficient of the 002 diffraction peak vs annealing temperature. (b) Homogeneous strain vs annealing temperature. (c) Williamson-Hall plot of ZnO thin films. (d) Inhomogeneous strain vs annealing temperature deduced from the Williamson-Hall plot. (e) Average crystallite size vs annealing temperature inferred from the Williamson-Hall plot.

Figure 4. Raman scattering spectra of ZnO thin films. The intensity is plotted in logarithm scale.

Figure 5. (a) Measured resistance vs distance in transmission line measurement and (b) deduced resistivity of ZnO thin films.

Figure 6. Topography of ZnO thin films (a) before and after being annealed at (b) 600, (c) 700, (d) 800, (e) 900 °C, and (f) 1000 °C. Piezoelectric amplitude of ZnO thin films (g) before and after being annealed at (h) 600, (i) 700, (j) 800, (k) 900 °C, and (l) 1000 °C. Piezoelectric phase of ZnO thin films (m) before and after being annealed at (n) 600, (o) 700, (p) 800, (q) 900 °C, and (r) 1000 °C.

Figure 7. Raw piezoelectric amplitude histograms of ZnO thin films (a) before and after being annealed at (b) 600, (c) 700, (d) 800, (e) 900 and (f) 1000 °C. Raw piezoelectric phase histograms of ZnO thin films (g) before and after being annealed at (h) 600, (i) 700, (j) 800, (k) 900 and (l) 1000 °C.

Figure 8. Piezoelectric amplitude histograms of ZnO thin films (a) before and after being annealed at (b) 600, (c) 700, (d) 800, (e) 900 and (f) 1000 °C after the data treatments.

Figure 9. Average piezoelectric amplitude on (a) Zn-polar and O-polar area, and (b) percentage of Zn-polar area of ZnO thin films.

Supplementary Information

Effects of Thermal Annealing on the Structural and Electrical Properties of ZnO Thin Films for Boosting their Piezoelectric Response

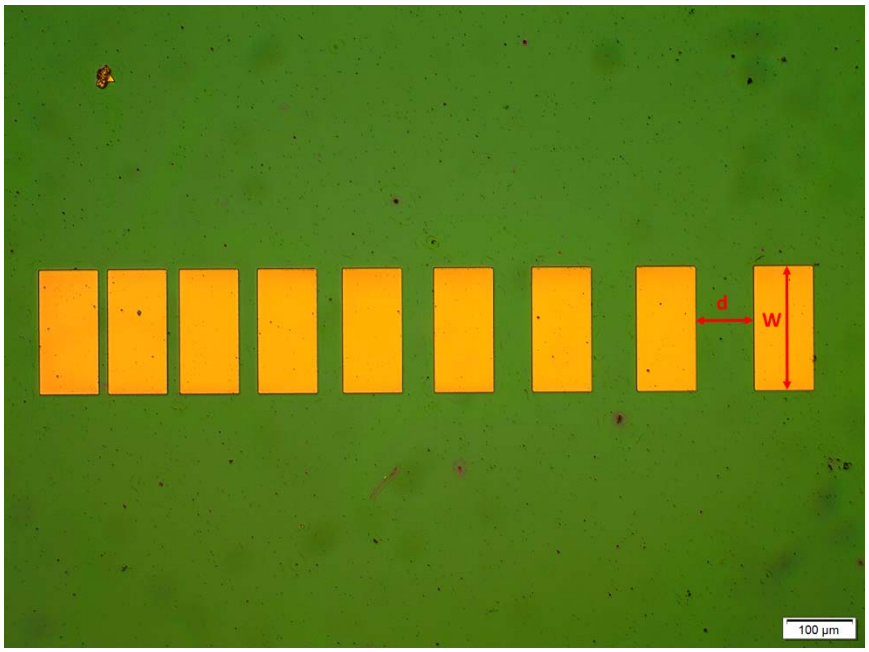

Figure S1. Series of metallic electrodes deposited on thin film surface.

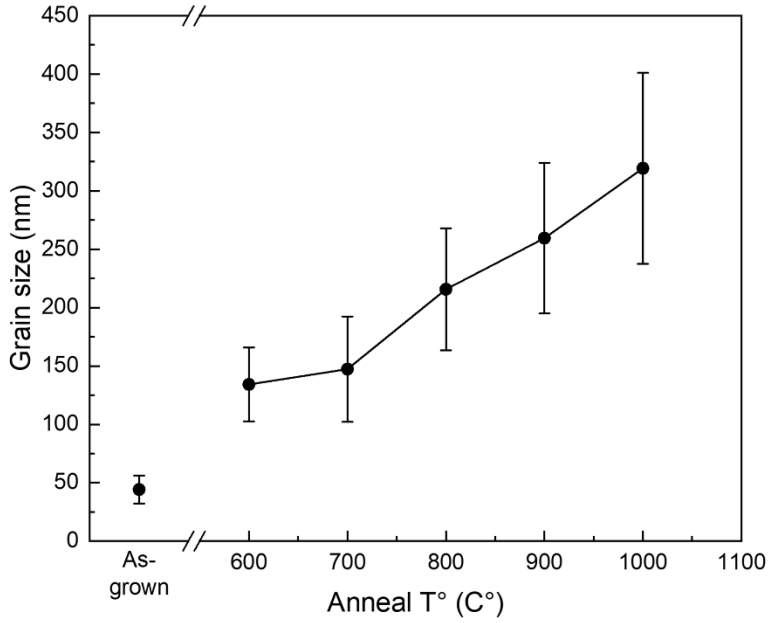

Figure S2. Average grain size of ZnO before and after being annealed at 600 – 1000 °C measured from top-view SEM images.

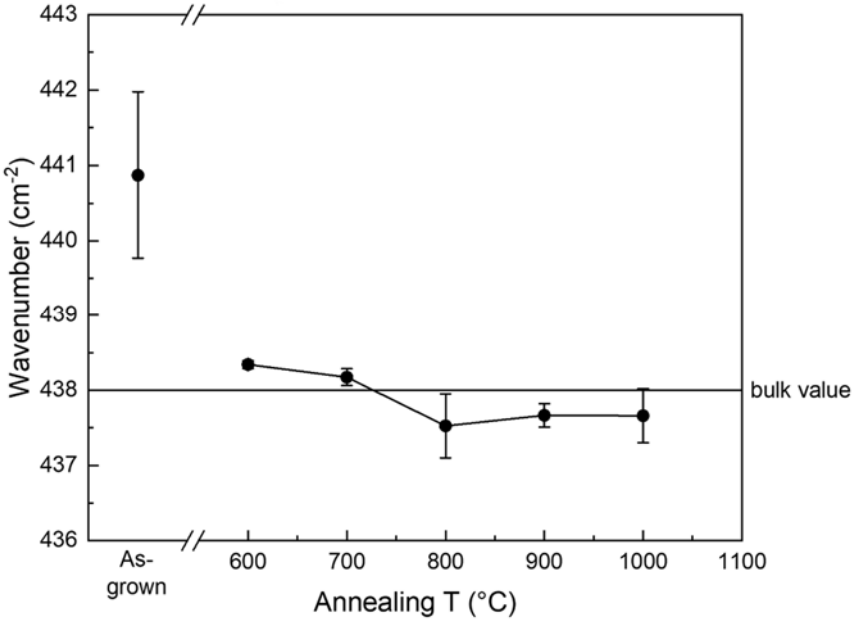

Figure S3. The E_2^{high} peak position in Raman spectra of ZnO before and after being annealed at 600 – 1000 °C.

Graphical Abstract